ADVANCED FUNCTIONAL MATERIALS
www.afm-journal.de

Enhanced Voltage-Controlled Magnetic Anisotropy and Field-Free Magnetization Switching Achieved with High Work Function and Opposite Spin Hall Angles in W/Pt/W SOT Tri-Layers

*Yu-Chia Chen, Qi Jia, Yifei Yang, Yu-Han Huang, Deyuan Lyu, Thomas J. Peterson, and Jian-Ping Wang**

Voltage-Gated Spin-Orbit-Torque (VGSOT) Magnetic Random-Access Memory (MRAM) is a promising candidate for reducing writing energy and improving writing speed in emerging memory and in-memory computing applications. However, conventional Voltage Controlled Magnetic Anisotropy (VCMA) approaches are often inefficient due to the low VCMA coefficient at the CoFeB/MgO interface. Additionally, traditional heavy metal/perpendicular magnetic anisotropy (PMA) ferromagnet bilayers require an external magnetic field to overcome symmetry constraints and achieve deterministic SOT switching. Here, a novel and industry-compatible SOT underlayer for next-generation VGSOT MRAM by employing a composite heavy metal tri-layer with a high work function is presented. This approach achieves a VCMA coefficient exceeding 100 fJ $V^{-1}m^{-1}$ through electron depletion effects, which is ten times larger than that observed with a pure W underlayer. Furthermore, it is demonstrated that this composite heavy metal SOT underlayer facilitates the integration of VCMA with opposite spin Hall angles, enabling field-free SOT switching in industry-compatible PMA CoFeB/MgO systems.

1. Introduction

Spintronic-based memory is a promising candidate for beyond-CMOS technology by leveraging the intrinsic spins of electrons alongside their charges, enabling faster and more power-efficient devices.[1–4] One notable technology in the spintronic-based memory realm is Spin-Transfer Torque (STT)-MRAM. STT-MRAM manipulates magnetic moments using a spin-polarized current instead of an external magnetic field, overcoming scaling limitations.[5–7] When a spin-polarized current flows through a ferromagnetic layer, it exerts a torque on the magnetic moments within the material.[8–10] However, reliability issues stemming from high-current stress on the interface have prompted research into SOT-MRAM, which originates from the spin Hall effect in heavy metals.[11,12]

SOT arises from spin accumulation at the interface between ferromagnetic and heavy metal layers, with spin current generation attributed to spin-orbit coupling (SOC) such as the spin Hall effect and the Rashba–Edelstein effect.[13–15] However, the torque generated solely by the SOT effective field is insufficient for flipping PMA magnetization and requires an external magnetic field. Therefore, various solutions have been proposed to break the symmetry and achieve field-free SOT switching, such as generating an in-plane internal effective field through antiferromagnetic interlayer exchange bias or interlayer exchange coupling, lateral structural asymmetry, low symmetry materials, opposite spin Hall angles materials, spin current gradient, lateral spin-orbit torques, and chiral magnetic domain wall.[16–27]

VCMA is a promising strategy to assist STT and SOT-MRAM in lowering energy consumption.[28,29] It operates by dynamically adjusting the energy barrier height at the interface between an insulator and a ferromagnetic layer using an external voltage bias through the intricate interplay between the electronic states of the ferromagnetic materials and the tunnel barrier.[30–32] Specifically, the dynamics of electron occupancy in the 3d orbitals of the ferromagnetic materials and the 2p

Y.-C. Chen, Q. Jia, Y. Yang, Y.-H. Huang, D. Lyu, J.-P. Wang
Electrical and Computer Engineering Department
University of Minnesota
Minneapolis, Minnesota 55455, USA
E-mail: jpwang@umn.edu
Y.-H. Huang
Department of Materials Science and Engineering
National Yang Ming Chiao Tung University
Hsinchu 30010, Taiwan
T. J. Peterson, J.-P. Wang
School of Physics and Astronomy
University of Minnesota
Minneapolis, Minnesota 55455, USA

The ORCID identification number(s) for the author(s) of this article can be found under https://doi.org/10.1002/adfm.202416570

DOI: 10.1002/adfm.202416570

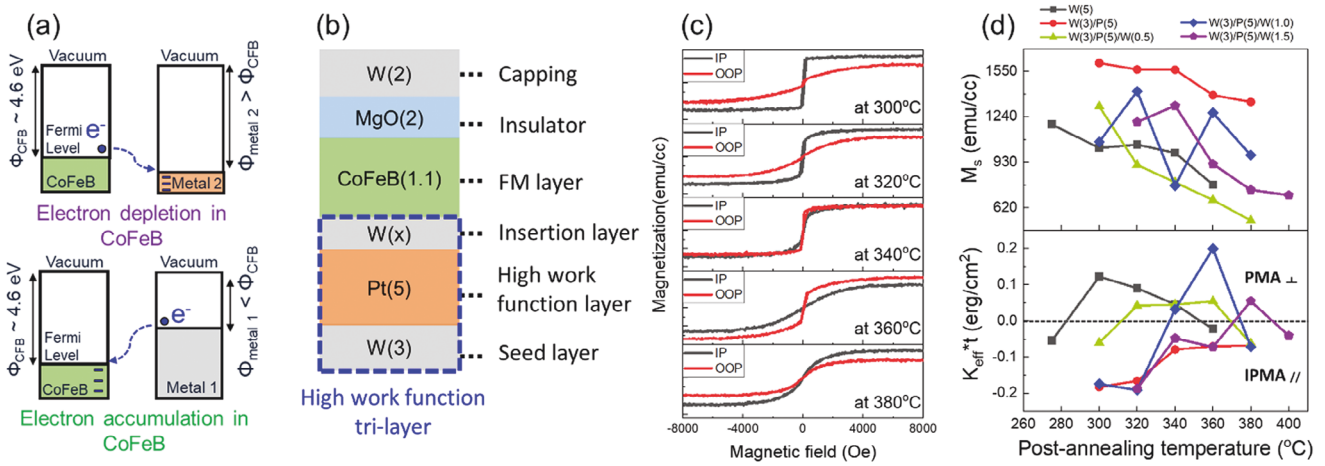

Figure 1. a) Band diagram illustrating electron accumulation and depletion in CoFeB (work function ≈4.6 eV) with metals of higher and lower work functions at thermal equilibrium. b) The validated tri-layer design aims to achieve electron depletion in the PMA CoFeB/MgO system by incorporating seeding, high work function, and insertion layers. c) VSM measurements for IP and OOP magnetization of CoFeB with varying thicknesses of W insertion layer. d) Saturation magnetization (M_s) and effective anisotropy constant (K_{eff}) with varying W insertion layers at different post-annealing temperatures for 20 min.

orbitals of the tunnel barrier are crucial in shaping the magnetic anisotropy.[33,34] However, this traditional VCMA approach is inefficient for supporting STT-MRAM and SOT-MRAM, which requires a VCMA coefficient >1000 and >300 fJ $V^{-1}m^{-1}$, respectively.[29]

In pursuit of enhancing VCMA, Zhang et al. theoretically proposed a bidirectional VCMA effect up to 1.1 pJ $V^{-1}m^{-1}$ in heavily electron-depleted Fe/MgO interfaces.[34] In a related study, Peterson et al. explored electron depletion levels in CoFeB by proposing and implementing a tri-layer underlayer material (Ta/Pd/Ta) with a tunable work function.[35] This approach effectively shifted the chemical potential at the CoFeB/MgO interface, leading to an enhanced VCMA response through the electron depletion mechanism, as validated by DFT calculations. The observed trend in VCMA suggested that the achieved electron depletion was insufficient, necessitating further exploration of underlayers with even higher work functions.

In this study, we explore a novel design strategy that incorporates high work function and high-electronegativity metals to induce VCMA through electron depletion at the PMA CoFeB/MgO interface and leverages opposite spin Hall angles in a tri-layer SOT channel to generate competing spin currents. Our investigation focuses on the W(3 nm)/Pt(5 nm)/W(x nm) underlayers in the CoFeB/MgO system. The electron depletion behavior at the CoFeB/MgO interface was confirmed using X-ray photoelectron spectroscopy (XPS) and ultraviolet photoelectron spectroscopy (UPS). Notably, the high work function of Pt in W(3 nm)/Pt(5 nm)/W(x nm) underlayer (W/Pt ~ 4.8/5.7 eV) plays a crucial role in enhancing the VCMA effect, showing an improvement of approximately ten times greater compared to a pure W underlayer. Besides, field-free magnetization switching was achieved in the W/Pt/W tri-layer by generating a perpendicular effective field through opposite spin Hall angles.

2. Results and Discussion

2.1. Concept of an Electron-Depletion VCMA Structure

As mentioned above, the VCMA effect can be enhanced via electron depletion from the CoFeB and MgO interface.[34] The potential SOT underlayers should have a high work function and strong electronegativity, both of which are larger than those of CoFeB (work function ≈4.6 eV and electronegativity ≈1.8). Among all metals, the Pt SOT channel best meets these requirements, possessing a work function of 5.7 eV and an electronegativity of 2.2.[36] **Figure 1a** illustrates the schematic of electron depletion and accumulation in CoFeB with metals of higher and lower work functions. A higher work function metal (>4.6 eV) increases the probability of electron depletion from CoFeB to the high work function underlayer at thermal equilibrium. In contrast, a lower work function metal (<4.6 eV) would more easily induce electron accumulation from the low work function underlayer to CoFeB. In addition, a strongly electronegative Pt atom more easily attracts bonding pair electrons from CoFeB.[36] Moreover, Pt has demonstrated strong damping-like torque efficiency for SOT applications.[37–39]

2.2. Integration of PMA CoFeB/MgO System With High Work Function Tri-Layer

The interfacial PMA in the CoFeB/MgO structure originates from the crystallization of CoFe at the CoFeB/MgO interface. This behavior is strongly influenced by the diffusion of boron (B) into the underlayer, as well as the diffusion of underlayer elements into the CoFeB layer during the post-annealing process.[40] Effective B diffusion into the underlayer, coupled with minimal underlayer element diffusion into the CoFeB layer, results in a more robust PMA. Based on this understanding, the diffusion of B, W, and Pt plays a crucial role in this study. It is challenging to

prepare CoFeB/MgO with robust PMA and tunneling magnetoresistance (TMR) on the Pt SOT channel due to the mismatched crystal structure of Pt with a face-centered cubic structure and crystallized CoFe with a body-centered cubic structure.[41–44] Besides, the adhesion between Pt and the SiO_2 substrate poses a fabrication issue. To address these challenges, we propose and validate a tri-layer design aimed at achieving electron depletion in the PMA CoFeB/MgO system by applying a 3 nm W seeding layer, a 5 nm Pt high work function layer, and various thicknesses (0/0.5/1.0/1.5 nm) of W insertion layers, as shown in Figure 1b.

To further explore the influence of W insertion layer on PMA, the W reference samples and high work function tri-layer samples with varying W insertion layers were post-annealed at different post-annealing temperatures for 20 min. Figures S1 and S2 (Supporting Information) display the in-plane (IP) and out-of-plane (OOP) magnetization measurements with the W(3 nm)/Pt(5 nm)/W(0/0.5/1.0/1.5 nm) SOT underlayer and the CoFeB/MgO system after post-annealing. For the W(5 nm) underlayer, weak PMA (no significant remanent polarization) was observed at 320 and 340 °C, with robust PMA achieved at 300 °C. In the W(3 nm)/Pt(5 nm)/W(0.5 nm) underlayer, weak PMA appeared at 320 and 340 °C. In Figure 1c, the W(3 nm)/Pt(5 nm)/W(1.0 nm) underlayer, weak PMA was seen at 340 °C, with robust PMA at 360 °C. Finally, for the W(3 nm)/Pt(5 nm)/W(1.5 nm) underlayer, weak PMA was observed at 380 °C. By analyzing the magnetization difference between IP and OOP, the saturation magnetization (M_s) and effective anisotropy energy (K_{eff}) can be obtained. A summary of the M_s and $K_{eff}*t_{CoFeB}$ from 275 to 400 °C is shown in Figure 1d. With the 1 nm W insertion layer, the M_s and $K_{eff}*t_{CoFeB}$ are 1265 emu cc^{-1} and 0.2 erg cm^2, respectively.

Based on these observations, we conclude that the W reference sample begins to exhibit PMA at lower temperatures compared to high work function Pt underlayers. This suggests that B and W elements start diffusing earlier, and the optimal balance of W and B diffusion occurs between 300 and 320 °C. In contrast, the Pt-based high work function tri-layers demonstrate PMA at higher temperatures as the W insertion layer increases. This indicates that either B or W preferentially diffuses into the Pt layer at elevated temperatures, with the Pt layer acting as the primary absorption layer for B. A plausible explanation for this phenomenon is that thicker insertion layers hinder the diffusion of B into the Pt underlayer. This detailed investigation highlights the critical balance between W layer thickness and its effects on the magnetic properties of the Pt/CoFeB and CoFeB/MgO interfaces, guiding the optimization of SOT devices.

2.3. Confirm the Electron Depletion by XPS & UPS

XPS and UPS were employed to examine the electronegativity properties and work functions.[45,46] The electron depletion at the CoFeB/MgO interface was demonstrated by the binding energy shift observed with high-resolution XPS (HR-XPS), as depicted in **Figure 2**. To precisely determine the binding energy shift at the CoFeB/MgO interface, all samples were analyzed using depth profiling HR-XPS, as shown in Figure S3 (Supporting Information). The interface between CoFeB and MgO was defined by the crossover points of the Mg 1s and Fe 2p signals. It also presents the atomic fractions of Pt at the CoFeB/MgO interface for various samples, which include W(3 nm)/Pt(5 nm)/W(0/0.5/1.0/1.5 nm). Figure S4 (Supporting Information) indicates that the thickness of the W insertion layer affects the degree of electron depletion and binding energy shift. Thicker W insertions result in higher W and lower Pt atomic fractions at the CoFeB/MgO interface, whereas thinner W insertions exhibit the opposite trend. This suggests that the thickness of the W insertion layer influences the extent of electron depletion at the CoFeB/MgO interface, likely due to the influence of the high work function and electronegativity of the tri-layer underlayer.

Figure 2a compares the binding energy shifts of the Fe 2p orbital between the W control sample and the W(3 nm)/Pt(5 nm)/W(1 nm) tri-layer sample. Notably, the W(3 nm)/Pt(5 nm)/W(1 nm) tri-layer exhibits a binding energy increase of ≈0.25 eV relative to the W control sample, indicating a reduction in electron density at the CoFeB/MgO interface. This shift suggests that the presence of the Pt layer in the tri-layer sample influences the electron distribution at the interface. Figures 2b,c summarize the binding energy shifts for the Fe 2p, W 4f, and Pt 4f orbitals with various thicknesses of the W insertion layer. The W(5 nm) and W(3 nm)/Pt(5 nm) underlayers are used as references for weak and strong electronegativity cases, respectively. The data show that the W(3 nm)/Pt(5 nm)/W(x nm) underlayers result in higher binding energy values for the Fe 2p and W 4f orbitals compared to the pure W underlayer. Specifically, the Fe $2p_{3/2}$ and W $4f_{7/2}$ orbital peaks shift to higher binding energies of 706.5/706.6/706.65/706.9 eV and 30.95/31.05/31.15/31.35 eV, respectively, with increasing thickness of the W insertion (1.5/1.0/0.5/0 nm) and a 5 nm Pt underlayer. In contrast, Figure 2c shows that the Pt 4f orbitals shift to lower binding energies, with the Pt $4f_{7/2}$ peak moving to 706.5/706.6/706.65/706.9 eV for 1.5/1.0/0.5/0 nm W insertions. All relative energy shift values are summarized in **Table 1**. These shifts highlight the influence of Pt's higher electronegativity in attracting electrons, thus altering the electronic structure and properties of the CoFeB/MgO interface. The results confirm that electron depletion can be controlled by adjusting the thickness of the W insertion layer between CoFeB and the Pt SOT channel. Additionally, UPS measurements show that the work functions of CoFeB, W, and Pt single layers are 4.6, 4.8, and 5.7 eV, respectively (Figure 2b). This suggests that at thermal equilibrium, electrons from W and CoFeB tend to occupy the lower energy levels of Pt due to their higher work function, which is consistent with the binding energy shift of Fe $2p_{3/2}$ revealed by HR-XPS.

2.4. Spin Torque Efficiency of the Tri-Layered Spin Hall Channel

The effect of the W insertion layers on SOT efficiency is investigated in this section. According to several studies, Ma et al. first demonstrated the field-free magnetization switching for the PMA ferromagnetic layer, which can be facilitated by the opposite spin Hall angles exhibited by W/Pt heavy metals, and attributed it to an intriguing interplay of competing spin currents.[21] Regarding the mechanism of competing spin currents, Ma et al. proposed that competing spin currents arise when materials with opposite spin Hall angles are integrated into the SOT layer. Through

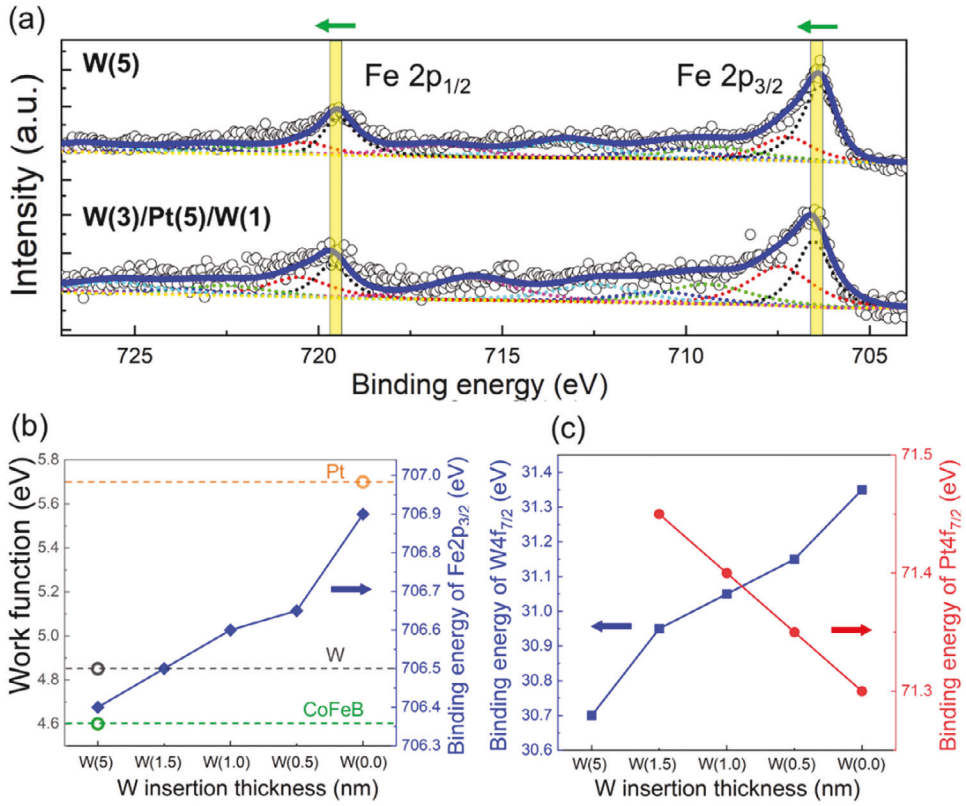

Figure 2. Electron depletion at the CoFeB/MgO interface as determined by XPS and UPS. a) Comparison of binding energy shifts of the Fe 2p orbital between the W control sample and the W(3 nm)/Pt(5 nm)/W(1 nm) sample. Summary of b) the work functions of CoFeB, W, and Pt, and the binding energy shifts of the Fe 2p orbital, and c) the binding energy shifts of the W 4f and Pt 4f orbitals with different W insertion layers on Pt SOT channels.

Magneto-Optical Kerr Effect (MOKE) measurements, they observed that domain wall velocities differ between downward and upward magnetization, driven by opposite spin Hall angles in the bilayer structure. This phenomenon is similar to the conventional SOT mechanism, which involves an in-plane magnetic field (H_x) that breaks ferromagnetic symmetry. Additionally, the observed loop shift suggests the presence of an effective perpendicular magnetic field, indicating the existence of an asymmetric domain wall. Specifically, the highest effective perpendicular magnetic field is generated when either the damping-like (DL) or field-like (FL) torque approaches zero. The origin of the competing spin currents or effective perpendicular magnetic field is believed to lie at the Pt and W interface, as demonstrated by the insertion of a 1 nm Au layer between the Pt and W layers.

Second harmonic measurements further reveal that the conventional SOT model does not fully explain the behavior for opposite spin Hall angles layered structure. Specifically, in the case of the highest effective perpendicular field, both the damping-like and field-like torques approach zero. This suggests that the current SOT model does not fully fit with field-free magnetization switching caused by opposite spin Hall angles layered structure. However, the conventional SOT model can still be used to predict and describe the potential for field-free SOT switching in these structures when combined with the results from loop shift measurements. Their findings suggest that loop shifts and second harmonic measurements can be useful tools for exploring the possibility of field-free switching in opposite spin Hall angle layered structures. Furthermore, subsequent studies demonstrated that a similar concept of competing spin currents can be realized

Table 1. Relative energy shift values of Fe 2p, W 4f, and Pt 4f orbitals with W control and W(3 nm)/Pt(5 nm)/W(x nm) samples.

Underlayer	Fe 2p [eV]	Relative Value [eV]	W 4f [eV]	Relative Value [eV]	Pt 4f [eV]	Relative Value [eV]
W(5)	706.4 (ref.)	0.0	30.7 (ref.)	0.0	NA	NA
W(3)/Pt(5)/W(1.5)	706.5	0.1	30.95	0.25	71.45	0.15
W(3)/Pt(5)/W(1)	706.6	0.2	31.05	0.35	71.4	0.1
W(3)/Pt(5)/W(0.5)	706.65	0.25	31.15	0.45	71.35	0.05
W(3)/Pt(5)	706.9	0.5	31.35	0.65	71.3 (ref.)	0.0

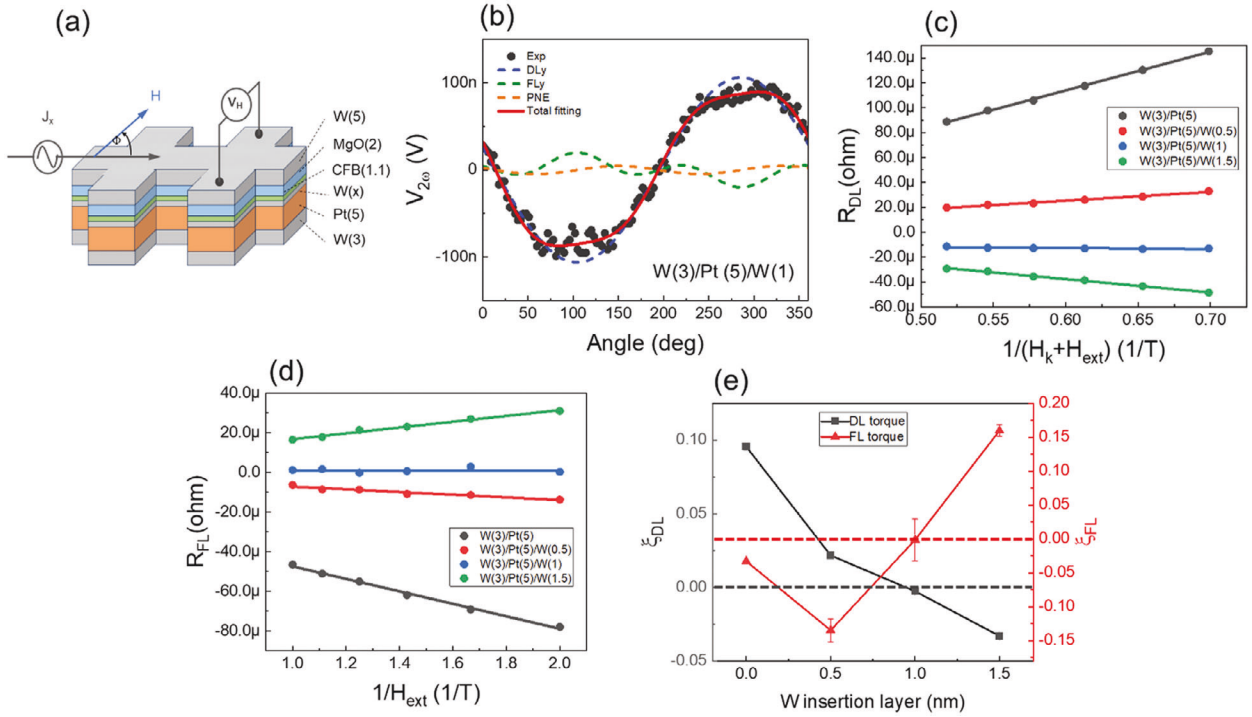

Figure 3. Second harmonic measurement for defining DL and FL SOT efficiency with different thicknesses of the W insertion layer. a) Schematic of the Hall bar device. b) Angular-dependent second harmonic Hall voltage of W(3 nm)/Pt(5 nm)/W(1 nm) sample. c) Linear fit of DL signal (Converted into resistance) and d) FL signal as a function of the inverse of the field. e) Extraction of SOT efficiency of samples with various W insertion layer thicknesses.

in Ta/Pd bilayer structure.[47] Even greater efficiency achieved using opposite spin Hall angles alloys such as PtGd, PtMo, and PtW.[48–51]

The design of the high-work function tri-layer structure is similar to that of a bilayer structure. In this study, we applied the methods of Ma et al., including second harmonic and loop shift measurements, to analyze the potential for field-free switching in W(3 nm)/Pt(5 nm)/W(x nm) high work function tri-layers. To explore the optimal interplay of competing spin currents, we investigated the DL and FL SOT efficiencies with different thicknesses of the W insertion layer on the 3 nm W seed layer/5 nm Pt SOT channel. In **Figure 3**, second harmonic measurements were conducted using two lock-in amplifiers. The angular dependence of Hall resistance was measured at different angles under the in-plane magnetic field and the driving current (7 mA at 133.7 Hz). The second harmonic signal can be expressed by:

$$V_{xy}^{2\omega} = \left[V_{DL}\cos(\varphi) - V_{FL}\cos(\varphi)\cos(2\varphi)\right] \quad (1)$$

$$V_{DL} = \frac{1}{2}R_{AHE}\frac{-H_{DL}}{H_{ext}+H_k} + I\alpha\nabla T \quad (2)$$

$$V_{FL} = R_{PHE}\frac{H_{FL}+H_{Oe}}{H_{ext}} \quad (3)$$

According to Equation (1), the second harmonic voltage can be divided into V_{DL} and V_{FL} with different magnetic fields, and the voltages are converted into resistance as shown in Figures 3c,d. Linear fitting with Equation (2) and Equation (3) allows for the estimation of the effective SOT field associated with DL and FL torques. The DL and FL SOT efficiencies are summarized in Figure 3e. The DL and FL torque of the W(3 nm)/Pt(5 nm) underlayer is calculated to be $\zeta_{DL} \sim +0.096 \pm 0.002$ and $\zeta_{FL} \sim -0.03 \pm 0.001$, respectively, indicating a Pt-dominated SOT efficiency compared with previous literature.[37–39] The spin diffusion length of Pt is shorter than 5 nm, suggesting that the spin current generated by the W seed layer does not diffuse into the CoFeB layer across the 5 nm Pt layer.[52,53] It implies that the competing spin currents originate from both the Pt high work function layer and the top W insertion layer.

The contribution of the DL torque gradually increases with the thickness of the W insertion layer. Both DL and FL torques in W(3 nm)/Pt(5 nm)/W(x nm) reverse sign when the W insertion layer reaches a thickness of ≈1 nm (x = 1 nm). Interestingly, both the DL and FL torque approach zero with a 1 nm W insertion layer, which are identified to be $\zeta_{DL} \sim$ -0.003 ± 0.001 and $\zeta_{FL} \sim$ -0.001 ± 0.03, respectively. These results are consistent with Ma et al.'s findings and indicate that competing spin currents can induce field-free SOT switching in W(3 nm)/Pt(5 nm)/W(1.0 nm) structures with opposite spin Hall angles.

2.5. Field-free SOT Switching and E-field Effects on Voltage-Gated Devices

To integrate electron depletion with high work function/electronegativity and enable field-free magnetization switching via competing spin currents in the PMA CoFeB/MgO system, a stack consisting of W(3 nm)/Pt(5 nm)/W(1 nm)/CoFeB(1.1 nm)/MgO(2 nm) was fabricated into a micron-sized pillar device

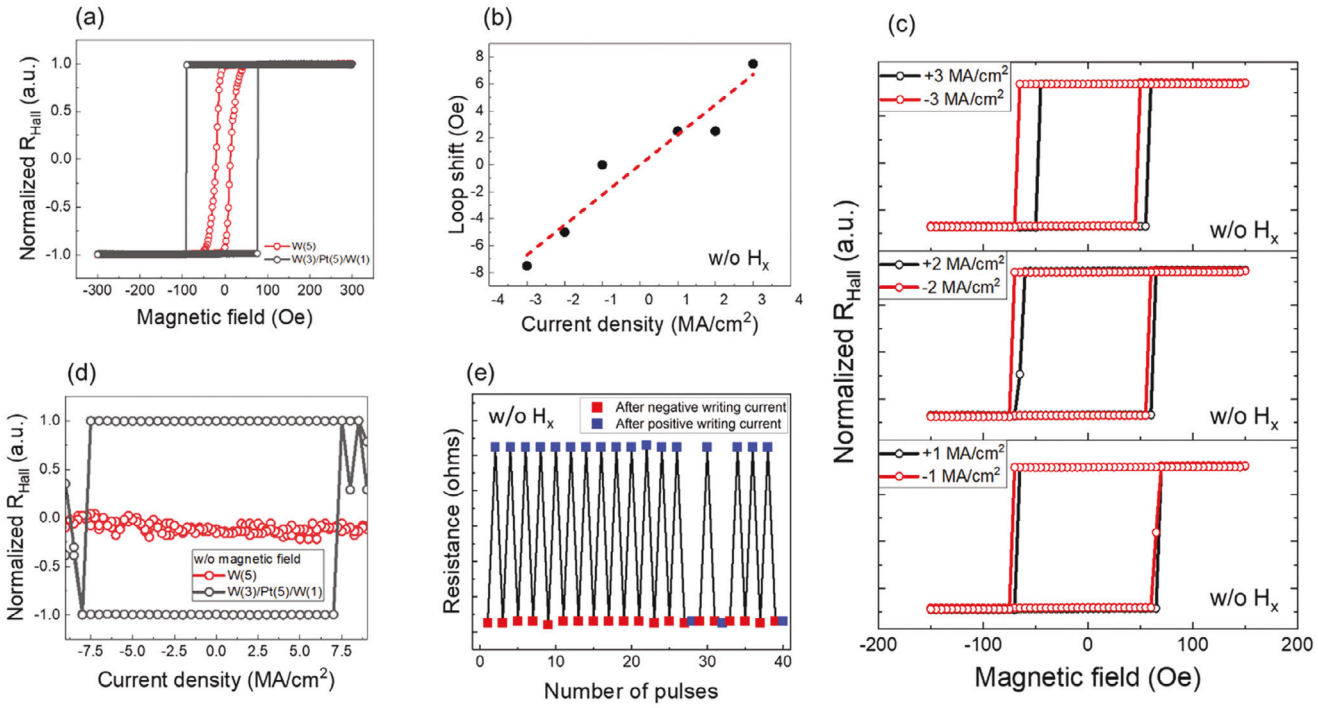

Figure 4. a) AHE measurement with an OOP magnetic field for the W control and W(3 nm)/Pt(5 nm)/W(1 nm) samples. b,c) Effective perpendicular field analysis at different magnitudes of applied current without the magnetic field of W(3 nm)/Pt(5 nm)/W(1 nm) sample. d) Field-free magnetization switching measurements for the W control and W(3 nm)/Pt(5 nm)/W(1 nm) samples. e) Field-free SOT switching stability testing of W(3 nm)/Pt(5 nm)/W(1 nm) sample.

(diameter = 9 μm). An additional 10 nm HfO_2 gate oxide was included for VCMA and SOT switching measurements. Other samples with varying W insertion thicknesses were not tested electrically for VCMA due to their weakened PMA.

Figure 4a depicts the PMA CoFeB/MgO system with W(5 nm) and W(3 nm)/Pt(5 nm)/W(1 nm) underlayers, assessed using the anomalous Hall effect (AHE) under a DC current and a perpendicular magnetic field ranging from −300 Oe to +300 Oe. The AHE voltages were normalized by setting the maximal (minimal) values to represent $M_z = +1$ (−1). The results reveal strong remnant magnetization and coercivity, in line with the VSM data, confirming a strong PMA. A perpendicular effective field was observed through the loop shift with varying current amplitudes and directions from -3 MA cm^{-2} to 3 MA cm^{-2}, without the magnetic field, as shown in Figure 4b. The loop shift is linearly proportional to the applied current, with a slope of ≈2.23 Oe mA^{-1}. Figure 4c shows the AHE measurements at +3/+2/+1 and −3/−2/−1 MA cm^{-2}, indicating a difference of ≈15/7.5/2.5 Oe. These findings also align with a related study.[21] Figure 4d presents field-free magnetization switching measurements using a 1 ms pulse current, comparing W control and W(3 nm)/Pt(5 nm)/W(1 nm) tri-layer samples. Achieving SOT switching typically requires breaking the symmetry of the magnetic layer, often by applying an in-plane magnetic field. Notably, the W(3 nm)/Pt(5 nm)/W(1 nm) configuration shows robust SOT magnetization switching without any magnetic field, with switching currents of ≈−7.5 and +7.5 MA cm^{-2}, whereas the W reference sample exhibits no switching behavior. Furthermore, stability testing of the field-free SOT switching, as shown in Figure 4e, involved applying positive and negative rectangular pulses over 40 pulses. The results demonstrate that the magnetization can switch stably and repeatedly between +1 and −1 states, with a switching probability of ≈92.5% under a 1 ms pulse width.

To evaluate the VCMA effect, in-plane AHE measurements were conducted with an additional gate voltage bias. The measurement setup is depicted in **Figure** 5a. By applying a magnetic field along the hard axis of the ferromagnetic material, the PMA energy per unit volume of the system (E_{eff}) can be defined and expressed as:

$$E_{eff} = \mu_0 M_s \int_0^1 H_x d\left(\frac{M_x}{M_s}\right) \tag{4}$$

where u_0 is the vacuum permeability, M_s is the saturation magnetization, H_x is the in-plane magnetic field along the x-axis, and M_x/M_s is the normalized in-plane magnetization. The relationship between E_{eff} and the effective CoFeB interfacial anisotropy (K_i) is described by the following equation:

$$K_i = E_{eff} * t_{CoFeB} + \mu_0 M_s^2/2 \tag{5}$$

where t_{CoFeB} is the thickness of CoFeB. Figure 5b presents the in-plane AHE measurements across a voltage ranging from −3 V to +3 V. The anomalous Hall resistance profiles clearly demonstrate gate-tunable anisotropy fields and effective magnetic anisotropy, with larger values observed under a negative electric field and smaller values under a positive one. Using the equations above, K_i can be calculated for each gate bias voltage. Figure 5c

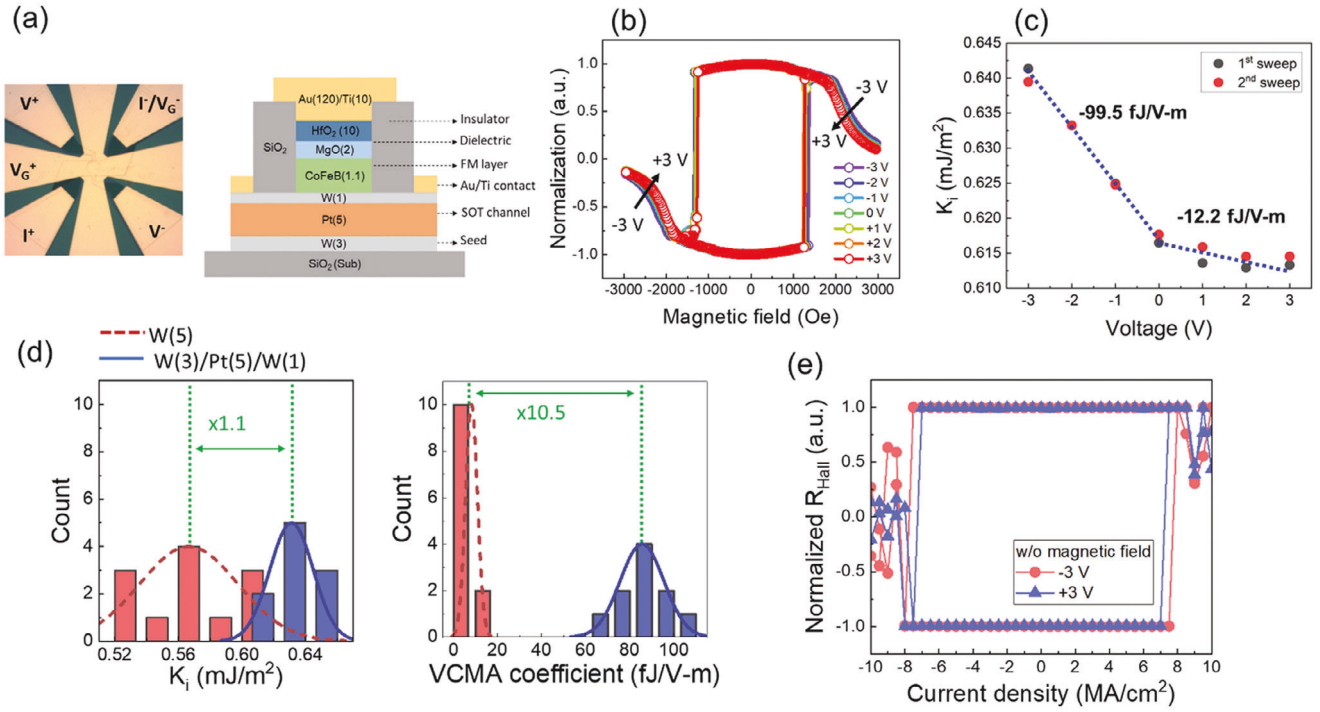

Figure 5. VGSOT measurement. a) Top view image and cross-section schematic of a micron-sized pillar device. b) Normalized IP AHE measurement with different bias voltages. c) Extracted interfacial effective anisotropy and linear fits of W(3 nm)/Pt(5 nm)/W(1 nm) insertion samples (black: first sweep for the linear fitting; red: second sweep). d) K_i and VCMA coefficient distributions of W control and W(3 nm)/Pt(5 nm)/W(1 nm) samples. e) Field-free VGSOT measurement under −3 V and +3 V.

illustrates the relationship between K_i and gate bias voltage for the W(3 nm)/Pt(5 nm)/W(1 nm) configuration. The VCMA coefficient is determined by the slope of K_i versus the gate voltage and can be expressed as:

$$\zeta_{VCMA} = d/d\left(\frac{V}{t_{gate}}\right) * K_i t_{CoFeB} \quad (6)$$

The VCMA linear fitting is divided into negative and positive electric field regimes due to their different slopes, which are −99.5 and −12.2 fJ $V^{-1}m^{-1}$, respectively. The variation in VCMA coefficients under different electric field directions is attributed to electron occupancy and de-occupancy properties at the CoFeB orbital. To further validate how electron depletion enhances VCMA, the W reference sample was tested using the same method. The distribution of K_i and VCMA coefficients for the W control and W(3 nm)/Pt(5 nm)/W(1 nm) tri-layer, measured over ten devices, is summarized in Figure 5d. The mean/highest of K_i value for the W(5 nm) sample is ≈0.57/0.60 mJ m^{-2}, while the mean/highest value for the W(3 nm)/Pt(5 nm)/W(1 nm) sample is ≈−0.63/0.64 mJ m^{-2}, indicating an enhancement of ≈10%. The mean/highest VCMA coefficient for the W(5 nm) sample is ≈−8.1/−11.0 fJ $V^{-1}m^{-1}$, while the mean/highest value for the W(3 nm)/Pt(5 nm)/W(1 nm) sample is ≈−85.6/−100.8 fJ $V^{-1}m^{-1}$, indicating an enhancement of ≈10 times. Finally, the VCMA pulse field-free SOT switching is shown in Figure 5e. The switching behavior was assessed using a 1 ms pulse-width current without an external magnetic field, under varying gate voltages. The difference in switching current between +3 and −3 V is ≈1 MA cm^{-2}, suggesting the potential for achieving lower switching currents with gate-tunable energy barriers.

We note that in field-free switching measurements, pronounced back-hopping effects are observed after magnetization switching, causing a magnetization transition from the high/low anomalous Hall resistance state to an approximately zero-anomalous Hall resistance state. Notably, these effects become more pronounced when a gate voltage is applied. Based on these observations, thermal fluctuations are likely a key factor contributing to the back-hopping effect. In SOT-based systems, back-hopping-like magnetization switching arises from the combined influence of spin-orbit torque and thermal effects.[54] When a pulse current with a 1 ms pulse width is applied, Joule heating is generated, which affects thermal fluctuations in the CoFeB layer, causing instability in the magnetization state and leading to back-hopping-like magnetization switching. Furthermore, the additional gate bias voltage increases Joule heating when the current passes through the HfO_2 and MgO insulators. As a result, more pronounced back-hopping effects are observed in voltage-gated SOT switching measurements.

Based on the above results, the high work function and opposite spin Hall angles in the W(3 nm)/Pt(5 nm)/W(1.0 nm) SOT tri-layer exhibit superior VGSOT performances. However, these results also suggest that the thickness threshold for achieving a high work function in the SOT tri-layer structure is quite narrow. Therefore, a key challenge for future applications is how to maintain PMA over a wider range of W insertion layer thicknesses. Several methods may be useful for improving PMA in this

regard, such as precise control of Mg insertions.[55,56] More flexible stack designs should also be considered, including high-work function alloys with opposite spin Hall angles, such as PtGd, PtMo, and PtW, which have already demonstrated field-free SOT switching.[48–50]

3. Conclusion

In summary, our study demonstrates a significant VCMA effect achieved through electron depletion and an efficienct field-free SOT switching of perpendicular magnetization by incorporating a high work function tri-layer with opposite spin Hall angles, specifically in the W(3 nm)/Pt(5 nm)/W(1 nm) configuration. This stack design holds substantial potential for advancing the understanding and practical implementation of VGSOT magnetization switching in spintronic devices.

4. Experimental Section

The W (3.0 nm)/Pt (5.0 nm)/W (x = 0, 0.5, 1.0, 1.5 nm)/$Co_{20}Fe_{60}B_{20}$ (1.1 nm)/MgO (2 nm)/W (2 nm) stacks were deposited on Si/SiO_2 substrates using an ultrahigh-vacuum magnetron sputtering system with a base pressure below 3×10^{-8} Torr at room temperature. The magnetic properties were characterized using a physical property measurement system (PPMS) equipped with a vibrating-sample magnetometer module.

The W (3.0 nm)/Pt (5.0 nm)/W (x = 0, 0.5, 1.0, 1.5 nm)/$Co_{20}Fe_{60}B_{20}$ (1.1 nm)/MgO (2 nm)/W (2 nm) samples were patterned into Hall bars with dimensions of 110 µm in length and 10 µm in width, as shown in Figure 3a. Metallic electrodes of Ti (10 nm)/Au (110 nm) were deposited using electron beam evaporation. An AC current with a frequency of 133 Hz and a peak value of 1 mA was applied through the channel by Keitheley 6221. The Hall bar was rotated in the xy plane from 0° to 360°, while the first- and second-harmonic Hall voltages were measured using two lock-in amplifiers (SR830).

The W (3.0 nm)/Pt (5.0 nm)/W (1.0 nm)/$Co_{20}Fe_{60}B_{20}$ (1.1 nm)/MgO (2 nm)/W (2 nm) samples were also patterned into VCMA+SOT pillar devices with a diameter of 4 µm, as shown in Figure 5a. During the patterning process, the 5 nm W capping layer was etched away by ion milling after post-annealing at 360 °C for 20 min. A 10 nm HfO_2 gate dielectric was then deposited at 70 °C using atomic layer deposition (ALD). Following this, metallic electrodes of Ti (10 nm)/Au (110 nm) were deposited by electron beam evaporation. The VCMA and field-free SOT switching were tested using a 5-probe method at room temperature.

Supporting Information

Supporting Information is available from the Wiley Online Library or from the author.

Acknowledgements

This work was partly supported by ASCENT, one of six centers in JUMP, a Semiconductor Research Corporation (SRC) program sponsored by DARPA, the Global Research Collaboration (GRC) Logic and Memory program, sponsored by SRC and NSF ASCENT TUNA program and NSF ASCENT TUNA: TUnable randomness for NAtural computing, No. 2230963. Parts of this work were carried out in the Characterization Facility, University of Minnesota, which receives partial support from the NSF through the MRSEC (Award Number DMR-2011401) and the NNCI (Award Number ECCS-2025124) programs. Portions of this work were conducted in the Minnesota Nano Center, which is supported by the National Science Foundation through the NNCI under Award Number ECCS-2025124.

Conflict of Interest

The authors declare no conflict of interest.

Data Availability Statement

The data that support the findings of this study are available from the corresponding author upon reasonable request.

Keywords

field-free magnetization switching, opposite spin Hall angles, spin-orbit torque material, voltage-controlled magnetic anisotropic, work function engineering

Received: September 5, 2024
Revised: October 25, 2024
Published online: November 20, 2024

[1] Z. Guo, J. Yin, Y. Bai, D. Zhu, K. Shi, G. Wang, K. Cao, W. Zhao, *Proc. IEEE* **2021**, *109*, 1398.
[2] S. A. Wolf, D. D. Awschalom, R. A. Buhrman, J. M. Daughton, S. Von Molnár, M. L. Roukes, A. Y. Chtchelkanova, D. M. Treger, *Science* **2001**, *294*, 1488.
[3] L. Guo, S. Hu, X. Gu, R. Zhang, K. Wang, W. Yan, X. Sun, *Adv. Mater.* **2024**, *36*, 2301854.
[4] J. P. Wang, S. S. Sapatnekar, C. H. Kim, P. Crowell, S. Koester, S. Datta, K. Roy, A. Raghunathan, X. S. Hu, M. Niemier, A. Naeemi, C. L. Chien, C. Ross, R. Kawakami, *Proc. of the 54th Annual Design Automation Conf.*, ACM, New York, **2017**, pp. 1–6.
[5] S. Bhatti, R. Sbiaa, A. Hirohata, H. Ohno, S. Fukami, S. N. Piramanayagam, *Mater. Today* **2017**, *20*, 530.
[6] J. Kim, A. Chen, B. Behin-Aein, S. Kumar, J. P. Wang, C. H. Kim, *IEEE Custom Integrated Circuits Conference (CICC)*, IEEE, New York, **2015**, pp. 1–4.
[7] S. C. Chang, N. Kani, S. Manipatruni, D. E. Nikonov, I. A. Young, A. Naeemi, *IEEE Trans. Magn.* **2016**, *52*, 1.
[8] E. Chen, D. Apalkov, Z. Diao, A. Driskill-Smith, D. Druist, D. Lottis, V. Nikitin, X. Tang, S. Watts, S. Wang, S. A. Wolf, A. W. Ghosh, J. W. Lu, S. J. Poon, M. Stan, W. H. Butler, S. Gupta, C. K. A. Mewes, T. Mewes, P. B. Visscher, *IEEE Trans. Magn.* **2010**, *46*, 1873.
[9] A. V. Khvalkovskiy, D. Apalkov, S. Watts, R. Chepulskii, R. S. Beach, A. Ong, X. Tang, A. Driskill-Smith, W. H. Butler, P. B. Visscher, D. Lottis, E. Chen, V. Nikitin, M. Krounbi, *J. Phys. Appl. Phys.* **2013**, *46*, 074001.
[10] S. Ikeda, J. Hayakawa, Y. M. Lee, F. Matsukura, Y. Ohno, T. Hanyu, H. Ohno, *IEEE Trans. Electron Devices* **2007**, *54*, 991.
[11] J. Ryu, S. Lee, K. Lee, B. Park, *Adv. Mater.* **2020**, *32*, 1907148.
[12] L. Zhu, *Adv. Mater.* **2023**, *35*, 2300853.
[13] R. Ramaswamy, J. M. Lee, K. Cai, H. Yang, *Appl. Phys. Rev.* **2018**, *5*, 031107.
[14] L. Liu, C. F. Pai, Y. Li, H. W. Tseng, D. C. Ralph, R. A. Buhrman, *Science* **2012**, *336*, 555.
[15] I. M. Miron, K. Garello, G. Gaudin, P. J. Zermatten, M. V. Costache, S. Auffret, S. Bandiera, B. Rodmacq, A. Schuhl, P. Gambardella, *Nature* **2011**, *476*, 189.
[16] S. Fukami, C. Zhang, S. DuttaGupta, A. Kurenkov, H. Ohno, *Nat. Mater.* **2016**, *15*, 535.
[17] Y. C. Lau, D. Betto, K. Rode, J. M. D. Coey, P. Stamenov, *Nat. Nanotechnol.* **2016**, *11*, 758.
[18] G. Yu, P. Upadhyaya, Y. Fan, J. G. Alzate, W. Jiang, K. L. Wong, S. Takei, S. A. Bender, L. T. Chang, Y. Jiang, M. Lang, J. Tang, Y. Wang, Y. Tserkovnyak, P. K. Amiri, K. L. Wang, *Nat. Nanotechnol.* **2014**, *9*, 548.

[19] D. MacNeill, G. M. Stiehl, M. H. D. Guimaraes, R. A. Buhrman, J. Park, D. C. Ralph, *Nat. Phys.* **2017**, *13*, 300.
[20] L. Liu, C. Zhou, X. Shu, C. Li, T. Zhao, W. Lin, J. Deng, Q. Xie, S. Chen, J. Zhou, R. Guo, H. Wang, J. Yu, S. Shi, P. Yang, S. Pennycook, A. Manchon, J. Chen, *Nat. Nanotechnol.* **2021**, *16*, 277.
[21] Q. Ma, Y. Li, D. B. Gopman, Y.u. P. Kabanov, R. D. Shull, C. L. Chien, *Phys. Rev. Lett.* **2018**, *120*, 117703.
[22] K. Cai, M. Yang, H. Ju, S. Wang, Y. Ji, B. Li, K. W. Edmonds, Y. Sheng, B. Zhang, N. Zhang, S. Liu, H. Zheng, K. Wang, *Nat. Mater.* **2017**, *16*, 712.
[23] Y. Cao, Y. Sheng, K. W. Edmonds, Y. Ji, H. Zheng, K. Wang, *Adv. Mater.* **2020**, *32*, 1907929.
[24] Z. Luo, T. P. Dao, A. Hrabec, J. Vijayakumar, A. Kleibert, M. Baumgartner, E. Kirk, J. Cui, T. Savchenko, G. Krishnaswamy, L. J. Heyderman, P. Gambardella, *Science* **2019**, *363*, 1435.
[25] Y. Sheng, W. Wang, Y. Deng, Y. Ji, H. Zheng, K. Wang, *Natl. Sci. Rev.* **2023**, *10*, nwad093.
[26] Y. Yang, S. Lee, Y.-C. Chen, Q. Jia, D. Sousa, M. Odlyzko, J. Garcia-Barriocanal, G. Yu, G. Haugstad, Y. Fan, Y.-H. Huang, D. Lyu, Z. Cresswell, T. Low, J.-P. Wang, Giant spin Hall effect with multi-directional spin components in Ni4W (Version 1). arXiv https://doi.org/10.48550/ARXIV.2411.05682.
[27] Y. Yang, S. Nair, S. Fan, Y. Chen, Y.-C. Jia, O. J. Benally, S. Lee, S. G. Jeong, Z. Yang, T. Low, B. Jalan, J.-P. Wang, **2024**, Coexistence of unconventional spin Hall effect and antisymmetric planar Hall effect in IrO$_2$ (Version 1). arXiv https://doi.org/10.48550/ARXIV.2411.05688.
[28] W. Kang, L. Chang, Y. Zhang, W. Zhao, *Design, Automation & Test in Europe Conference & Exhibition (DATE)*, IEEE, New York **2017**, pp. 542–547.
[29] Y. C. Wu, K. Garello, W. Kim, M. Gupta, M. Perumkunnil, V. Kateel, S. Couet, R. Carpenter, S. Rao, S. Van Beek, K. K. Vudya Sethu, F. Yasin, D. Crotti, G. S. Kar, *Phys. Rev. Appl.* **2021**, *15*, 064015.
[30] W. G. Wang, M. Li, S. Hageman, C. L. Chien, *Nat. Mater.* **2012**, *11*, 64.
[31] H. Cai, W. Kang, Y. Wang, L. Naviner, J. Yang, W. Zhao, *Appl. Sci.* **2017**, *7*, 929.
[32] T. Nozaki, T. Yamamoto, S. Miwa, M. Tsujikawa, M. Shirai, S. Yuasa, Y. Suzuki, *Micromachines* **2019**, *10*, 327.
[33] K. Klyukin, G. Beach, B. Yildiz, *Phys. Rev. Mater.* **2020**, *4*, 104416.
[34] J. Zhang, P. V. Lukashev, S. S. Jaswal, E. Y. Tsymbal, *Phys. Rev. B.* **2017**, *96*, 014435.
[35] T. J. Peterson, A. Hurben, W. Jiang, D. Zhang, B. Zink, Y. C. Chen, Y. Fan, T. Low, J. P. Wang, *J. Appl. Phys.* **2022**, *131*, 153904.
[36] S. Trasatti, *J. Electroanal. Chem. Interfacial Electrochem.* **1971**, *33*, 351.
[37] L. Zhu, D. C. Ralph, R. A. Buhrman, *Appl. Phys. Rev.* **2021**, *8*, 031308.
[38] H. Hayashi, A. Musha, H. Sakimura, K. Ando, *Phys. Rev. Res.* **2021**, *3*, 013042.
[39] J. W. Lee, Y. W. Oh, S. Y. Park, A. I. Figueroa, G. Van Der Laan, G. Go, K. J. Lee, B. G. Park, *Phys. Rev. B.* **2017**, *96*, 064405.
[40] G. G. An, J. B. Lee, S. M. Yang, H. S. Park, W. S. Chung, J. G. Park, J. P. Hong, *Acta Mater.* **2016**, *110*, 217.
[41] M. Akyol, B. Kıvrak, K. U. Tümen, A. Ekicibil, *J. Mater. Sci. Mater. Electron.* **2020**, *31*, 23037.
[42] M. Akyol, *J. Supercond. Nov. Magn.* **2019**, *32*, 457.
[43] W. Du, M. Liu, G. Wang, H. Su, B. Liu, H. Meng, X. Tang, *J. Alloys Compd.* **2022**, *928*, 167205.
[44] P. J. Chen, Y. L. Iunin, S. F. Cheng, R. D. Shull, *IEEE Trans. Magn.* **2016**, *52*, 1.
[45] D. C. Frost, A. Ishitani, C. A. McDowell, *Mol. Phys.* **1972**, *24*, 861.
[46] M. G. Helander, M. T. Greiner, Z. B. Wang, Z. H. Lu, *Appl. Surf. Sci.* **2010**, *256*, 2602.
[47] B. R. Zink, D. Zhang, H. Li, O. J. Benally, Y. Lv, D. Lyu, J. Wang, *Adv. Electron. Mater.* **2022**, *8*, 2200382.
[48] Z. A. Bekele, X. Liu, Y. Cao, K. Wang, *Adv. Electron. Mater.* **2021**, *7*, 2000793.
[49] X. Liu, X. Lan, Z. A. Bekele, W. Li, S. Zhu, P. Dou, Y. Wang, J. Zhang, S. Wang, K. Wang, *IEEE Trans. Nanotechnol.* **2023**, *22*, 576.
[50] Z. A. Bekele, R. Li, Y. Li, Y. Cao, X. Liu, K. Wang, *Adv. Electron. Mater.* **2021**, *7*, 2100528.
[51] X. Lan, X. Liu, Z. A. Bekele, K. Lei, K. Wang, *Appl. Phys. Lett.* **2023**, *122*, 172402.
[52] M. Isasa, E. Villamor, L. E. Hueso, M. Gradhand, F. Casanova, *Phys. Rev. B.* **2015**, *91*, 024402.
[53] J. C. Rojas-Sánchez, N. Reyren, P. Laczkowski, W. Savero, J. P. Attané, C. Deranlot, M. Jamet, J. M. George, L. Vila, H. Jaffrès, *Phys. Rev. Lett.* **2014**, *112*, 106602.
[54] R. Ren, Y. Cao, C. Wang, Y. Guan, S. Liu, L. Wang, Z. Du, C. Feng, Z. A. Bekele, X. Lan, N. Zhang, G. Yang, L. Wang, B. Li, Y. Hu, Y. Liu, S. Parkin, K. Wang, G. Yu, *Nano Lett.* **2024**, *24*, 10072.
[55] C. A. Pandey, X. Li, H. Wang, H. Wang, Y. Liu, H. Zhao, Q. Yang, T. Nie, W. Zhao, *J. Magn. Magn. Mater.* **2020**, *511*, 166956.
[56] X. Li, K. Fitzell, D. Wu, C. T. Karaba, A. Buditama, G. Yu, K. L. Wong, N. Altieri, C. Grezes, N. Kioussis, S. Tolbert, Z. Zhang, J. P. Chang, P. Khalili Amiri, K. L. Wang, *Appl. Phys. Lett.* **2017**, *110*, 052401.